Title

Tuning the Properties of Zero-Field Room Temperature Ferromagnetic Skyrmions by Interlayer Exchange Coupling.

Journal

Nano letters, 20(7)

ISSN

1530-6984

Authors

Lo Conte, Roberto
Nandy, Ashis K
Chen, Gong
et al.

Publication Date

2020-07-01

DOI

10.1021/acs.nanolett.0c00137

Peer reviewed

Tuning the properties of zero-field room temperature ferromagnetic skyrmions by interlayer exchange coupling

Roberto Lo Conte[*,1,2], *Ashis K. Nandy*[*,3], *Gong Chen*[4], *Andre L. Fernandes Cauduro*[5], *Ajanta Maity*[3], *Colin Ophus*[5], *Zhijie Chen*[6], *Alpha T. N'Diaye*[7], *Kai Liu*[4,6], *Andreas K. Schmid*[*,5], *and Roland Wiesendanger*[*,2]

[1]Department of Materials Science and Engineering, University of California, Berkeley, CA 94720, USA

[2]Department of Physics, University of Hamburg, D-20355 Hamburg, Germany

[3]School of Physical Sciences, National Institute of Science Education and Research, HBNI, P.O. Jatni, 752050, India

[4]Department of Physics, University of California, Davis, CA 95616, USA

[5]National Center for Electron Microscopy, Molecular Foundry - Lawrence Berkeley National laboratory, Berkeley, CA 94720, USA

[6]Physics Department, Georgetown University, Washington, DC 20057, USA

[7]Advanced Light Source, Lawrence Berkeley National Lab, Berkeley, CA 94720, USA

ABSTRACT: Magnetic materials offer an opportunity to overcome the scalability and energy consumption limits affecting the semiconductor industry. New computational device architectures, such as low-power solid state magnetic logic and memory-in-logic devices, have been proposed which rely on the unique properties of magnetic materials. Magnetic skyrmions, topologically protected quasi-particles, are at the core of many of the newly proposed spintronic devices. Many different materials systems have been shown hosting ferromagnetic skyrmions at room temperature. However, a magnetic field is a key ingredient to stabilize skyrmions, and this is not desirable for applications, due to the poor scalability of active components generating magnetic fields. Here we report the observation of ferromagnetic skyrmions at room temperature and zero magnetic field, stabilized through interlayer exchange coupling (IEC) between a *reference magnet* and a *free magnet*. Most importantly, by tuning the strength of the IEC we are able to tune the skyrmion size and areal density. Our findings are relevant to the development of skyrmion-based spintronic devices suitable for general-use applications which go beyond modern nanoelectronics.

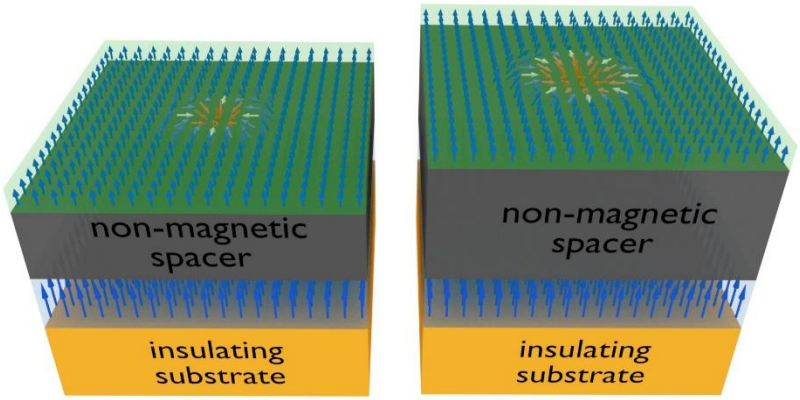

KEYWORDS: ferromagnetic skyrmions, non-collinear magnetism, interlayer exchange coupling, nanomagnetism, spintronics

The stabilization of magnetic skyrmions[1–4] in thin-films with perpendicular magnetic anisotropy (PMA) results from the competition among different energy terms. Depending on the balance between the Heisenberg exchange interaction, the antisymmetric exchange called the Dzyaloshinskii-Moriya interaction (DMI)[5–9], and the magnetic anisotropy a particular magnetic multilayer can have a ferromagnetic or a spin spiral ground state. When the DMI is sufficiently strong, helical – called Bloch-type – spin textures are suppressed in favor of cycloidal – called Néel-type – spin textures. In both of those ground states, the cycloidal spin-textures are limited to one specific sense of rotation (left-handed or right-handed)[8,10] determined by the DMI sign. In the specific case of a ferromagnetic ground state, which is relevant for this work, magnetic domains are separated by Néel-type domain walls (DWs) with a unique rotational sense, as shown in Fig. 1a. Finally, if a magnetic field is applied along the anisotropy axis of such system, isolated magnetic skyrmions can be nucleated[4] (Fig. 1b).

Thin film-based multilayers are particularly attractive for the design of potential skyrmionic devices[11–14], due to the high tunability of their magnetic properties through materials and structural engineering. So far, room-temperature ferromagnetic skyrmions have been observed in many different multilayers[15–21]. In order to make those material systems employable for spintronic applications[12,14,22], skyrmions must be stable without any external magnetic field. As a consequence, in the last few years different approaches to stabilize zero-field skyrmions have been developed[23–28]. Those approaches are based on lateral confinement[23,24], current pulses-induced morphological thermal transitions[26], exchange bias[27] and interlayer exchange coupling[25,29]. The latter two approaches seem to be more suitable for practical applications, since they allow lateral transport of skyrmions and do not rely on complicated post-growth initialization processes. Furthermore, the interlayer exchange coupling is preferable to the exchange bias approach due to

the tunability of the coupling and thus of the stabilized skyrmions. However, a systematic approach to fine-tune the properties of magnetic skyrmions in the absence of external magnetic fields is still missing.

Here, we report the fine-tuning of the size and areal density of ferromagnetic skyrmions at room temperature in epitaxial metallic multilayers, in the absence of external magnetic fields. The epitaxial multilayers are grown on top of insulating MgO single crystals, which makes them suitable for application in spintronic devices. The mechanism used for the stabilization of the skyrmions is interlayer exchange coupling[25,29–32]. By connecting two magnetic layers through a non-magnetic spacer, the indirect exchange coupling between the two magnetic layers is exploited in order to stabilize skyrmions at room temperature. A schematic of the multilayers investigated here is shown in Fig. 1c. At the bottom of the stack there is a thick ferromagnetic reference layer in a single domain state having all its magnetic moments pointing in the same direction. At the top of the stack there is a thinner magnetic free layer which, therefore, is subject to an effective magnetic field due to the magnetization of the reference layer. By changing the thickness of the non-magnetic spacer in between the two magnets we are able to tune the strength of the effective magnetic field, which allows us to tailor the properties of the skyrmions in the free layer.

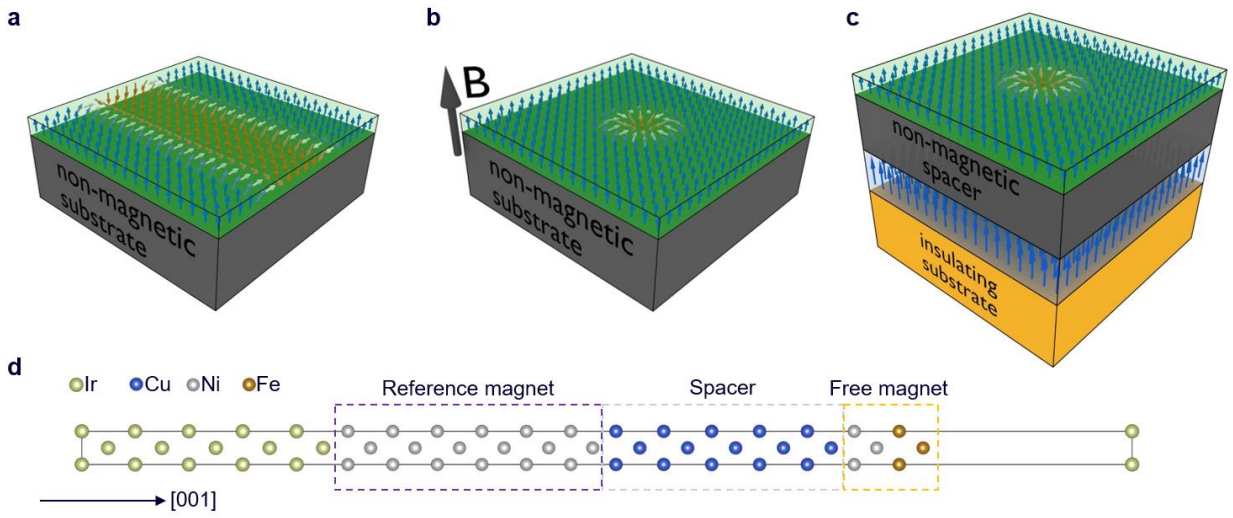

e

		a_{Ir} = 3.84 Å d_{Ir} = 2.72 Å	a_{Cu} = 3.61 Å d_{Cu} = 2.55 Å	a_{Ni} = 3.52 Å d_{Ni} = 2.49 Å
MCA: $E_{100} - E_{001}$ >0 → PMA (meV)	Ir(10)**Ni(12)**\\Cu(8)	0.31	0.40	0.18
	Cu(10)\\Ni(2)**Fe(1[2])**	0.55 [-0.008]	-0.098 [0.305]	-0.222 [0.154]

f

	a_{Cu} = 3.61 Å d_{Cu} = 2.55 Å		a_{Ni} = 3.52 Å d_{Ni} = 2.49 Å	
Cu spacer thickness (ML)	1/2*(E_{afm}-E_{fm}) (meV)	B_{eff} (T)	1/2*(E_{afm}-E_{fm}) (meV)	B_{eff} (T)
8	-0.1283	-0.351	0.0726	0.2
10	-0.1158	-0.317	0.2160	0.597
12	-0.1810	-0.495	-0.4163	-1.15
14	-0.0476	-0.13	-0.2004	-0.554
16	0.064	0.175		
18	0.234	0.64		

Figure 1. Interlayer exchange coupling stabilization of ferromagnetic skyrmions. a Schematic of a magnetic thin film hosting chiral domain walls due to interfacial DMI. **b** Stabilization of magnetic skyrmion via an external magnetic field. **c** Stabilization of magnetic skyrmion via IEC. **d** Schematic of the multilayer stack investigated by density functional theory calculations. **e** Calculated magneto-crystalline anisotropy energies for the *reference* and the *free* magnet. Three different calculations are carried out assuming an in-place lattice spacing (d_i) for the stack equal to that of Ir, Cu and Ni, respectively. Light blue boxes indicate the values corresponding to the calculation parameters expected to be the closest to the experimental scenario. **f** Calculated IEC and corresponding effective magnetic field acting on the free magnet (B_{eff}) as a function of the Cu spacer thickness, for two cases with in-plane lattice spacing equal to that of bulk Cu and Ni, respectively.

Using density functional theory (DFT) calculations as implemented in VASP package[33,34] we study the magnetic properties of the material stack Ir(10)\Ni(12)\Cu(t_{Cu})\Ni(2)\Fe(1-2), where the thicknesses are expressed in monolayer (ML). The material system is assumed to be in a face centered cubic (fcc) structure, with the stacking along the [001] crystallographic direction, as schematically shown in Fig. 1d. The materials stack is simulated for three different conditions, where the in-plane lattice constant (bulk lattice constant) is assumed to be equal to d_{Ir} = 2.72 Å (a_{Ir}

= 3.84 Å), d_{Cu} = 2.55 Å (a_{Cu} = 3.61 Å), d_{Ni} = 2.49 Å (a_{Ni} = 3.52 Å) for Ir, Cu and Ni, respectively. More details concerning the DFT calculations are reported in supplementary section S1. The table in Fig. 1e shows the calculated magneto-crystalline anisotropy (MCA) for the two magnetic layers. The bottom magnet Ir(10)\Ni(12)\Cu(8) is predicted to have PMA, regardless of the chosen in-plane lattice constant (and Cu thickness, data not shown here). On the other hand, the Cu(10)\Ni(2)\Fe(1-2) magnet is found to have a MCA which depends on the chosen in-plane lattice constant and the thickness of the Fe layer. As reported in the light blue box (results for calculation parameters expected to be most closely related to experimental conditions), the free magnet is predicted to have an in-plane MCA for t_{Fe} = 1 ML and an out-of-plane MCA for t_{Fe} = 2 ML. Furthermore, Fig. 1f shows the calculated IEC and corresponding effective magnetic field (B_{eff}) as a function of the Cu spacer thickness. The calculations show that an interlayer exchange coupling is expected to be present in the system, with a strength that can be tuned by tailoring the thickness of the spacer. Interestingly, calculations for stacks with different in-plane lattice spacing show different results. Therefore, we expect the actual in-plane lattice constant in the prepared stacks to play a very important role, especially in determining the sign of the IEC, ferromagnetic (>0) or antiferromagnetic (<0).

In order to understand the stability mechanism of magnetic DWs with a unidirectional sense of the spin rotation in the Ni(2)\Fe(2) free layer, we perform total energy calculations of flat homogeneous spin spirals (SS) characterized by SS vector **q** along the ΓM high symmetry line in the irreducible two-dimensional Brillouin Zone. Our first-principle calculations are based on the full-potential linearized augmented plane wave (FLAPW) method in the film geometry as implemented in FLEUR code[35] (see supplementary section S1 for more details). The effective spin model describing the free magnetic layer is comprised of the exchange interaction, DMI and MCA.

The exchange and the DMI constants both are the effective nearest neighbor interactions, where the former one is obtained by fitting the dispersion curve E(**q**) of SSs in the vicinity of the ferromagnetic (FM) state (**q** = 0) without spin-orbit coupling (SOC) while the latter is the result of relativistic effects within our SOC calculations. In the magnetic multilayer Cu(001)\Ni(2)\Fe(2), it is convenient to define intralayer exchange coupling, J^{FF} and J^{NN}, for the Fe(2) layer and the Ni(2) layer on Cu(001) substrate, respectively and an interlayer coupling, J^{FN}, at the Ni\Fe interface. The results of our calculations for the exchange interaction and DMI constants (see supplementary section S1 for more details) are summarized in Fig. 2. The SS calculations without SOC show a ferromagnetic ground state for both the magnetic layers and the full Cu(001)\Ni(2)\Fe(2) system. The effective intralayer exchange constant within the Fe(2) layer, J^{FF} = 31.1 meV is much stronger than that in the Ni(2) layer, J^{NN} = 3.2 meV; and the effective exchange constant for the full system is found to be J_{eff} = 46.2 meV. However, with inclusion of SOC the systems show non-collinear ground states with opposite rotational sense, left-handed for the Fe(2) layer and right-handed for the Ni(2) layer. The DMI in Ni(2), D^{NN} = 1.2 meV, is stronger than that in the Fe(2) layer, D^{FF} = -0.88 meV. Because of the C_{4v} symmetry of the film geometry, the DMI vectors around an atom are perpendicular to the bond connecting its nearest-neighbor atoms. Therefore, only Néel-type modulation of magnetizations (cycloidal SS) are supported. Fig. 2a shows the dispersion curve for each magnetic layer and the full system. The energy minima show that the SS state in the Ni(2) layer is robust and the SS period is small compare to that in the Fe(2) layer. Interestingly, the ferromagnetic interlayer exchange coupling, J^{FN} = 13.5 meV, along with the layer resolved DMI constants, D^{FF} and D^{NN}, support the prediction of a magnetic state in the full system which has a right-handed rotational sense, see inset of Fig. 2a. Indeed, all these energy contributions effectively stabilize a cycloidal SS ground state in the free layer, with a

rotation period λ = 205 nm. The effective DMI for the full system calculated within DFT is D_{eff} = 0.32 meV (0.16 meV per atom), in good agreement with the previously reported experimental estimation, 0.12 – 0.17 meV per atom, by G. Chen et al[36] for the materials system Cu(001)\Ni\Fe.

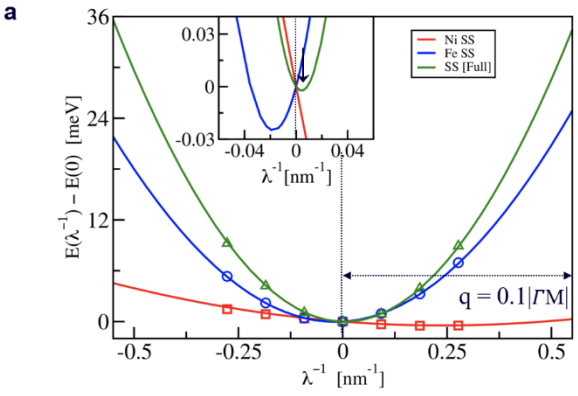

b

Cu(001)/Ni(2)/Fe(2)	Fe(2) Intralayer (J^{FF}, D^{FF})	Ni(2) intralayer (J^{NN}, D^{NN})	Ni(2)\Fe(2) Interlayer (J^{FN})	Ni(2)\Fe(2) intralayer (J_{eff}, D_{eff})
J_{nn} (meV)	31.1	3.2	13.5	46.2
D_{nn} (meV)	-0.88	1.2		0.32

Figure 2. Dzyaloshinskii-Moriya interaction calculations a. Energy dispersion E(**q**) of the spin-spiral (SS) as a function of λ^{-1} ($q/2\pi$ in nm^{-1}) along high symmetry line ΓM. The continuous lines correspond to the total energy from the model with effective exchange constant and DMI which are obtained by fitting the SS energy without SOC and layer resolved SOC contributions, respectively. The symbols are the calculated energy points close to the Γ-point. Red, blue and green refers to Ni(2), Fe(2) and Ni(2)\Fe(2), respectively. The black arrow in the inset denotes the lowest energy state of the full system. **b**. Effective nearest neighbor exchange constants, J_{nn} (J^{FF}, J^{NN}, J^{FN}, J_{eff}), and DMI, D_{nn} (D^{FF}, D^{NN}, D_{eff}), obtained from fitting the energy dispersion of SSs calculated within DFT without and with SOC, respectively. The intralayer exchange constants are calculated assuming effectively one atom model for the Fe(2), Ni(2) and full Cu(001)\Ni(2)\Fe(2) layers. The effective values for the full stack are reported in the last column on the right.

Next, we experimentally investigate the materials stack described above by *in-situ* imaging in a spin-polarized low energy electron microscope (SPLEEM). The *in-situ* capabilities of the SPLEEM allow us to observe the evolution of the magnetic state of the layer during growth as a function of its thickness. The out-of-plane (OOP)-magnetized reference magnet made of 12 ML

of Ni is deposited on an Ir(001)-(1x1) buffer layer grown on top of an insulating MgO(001) single crystal substrate (see schematic in Fig. 3a). Once the Ni layer is deposited, we saturate its magnetization state with an external magnetic field of $\mu_0 \boldsymbol{H}$ = -0.5 T, resulting in a single domain state with magnetic moments pointing down. Afterwards, we deposit the Cu spacer and finally the top magnet, which consists of 2 ML of Ni, and ~2.0-2.5 ML of Fe.

We begin our experimental investigation by exploring the interlayer coupling in this materials system. This is done by imaging the OOP magnetic state of the Ni(2)\Fe(2.5) free layer as a function of the thickness of a wedge-shaped Cu spacer, t_{Cu} (details about the growth of the wedged Cu spacer are available in the supplementary section S9). It is worth noting that, in agreement with the DFT calculations, a PMA is obtained only for $t_{Fe} > 1$ ML, allowing us to observe OOP-domains for t_{Fe} = 1.5-2.5 ML (no OOP contrast is observed for $t_{Fe} \leq 1$ ML). The investigation of the wedged sample reveals the presence of a ferromagnetic coupling between the two magnets over the entire range of the Cu-wedge thickness (0-35 ML), with a strength that varies as a function of t_{Cu}. In Fig. 3b, we report the normalized difference between the fractional areas of ferromagnetically (FM) and anti-ferromagnetically (AFM) coupled domains, (FM-AFM)/(FM+AFM) observed in a 10 μm field-of-view, as a function of t_{Cu}. This ratio gives us information about the sign (>0, ferromagnetic; <0, anti-ferromagnetic) and the varying strength of the interlayer coupling between free and reference magnets. As visible in the graph in Fig. 3b, even if the sign of the IEC is the same for all the investigated t_{Cu}, its amplitude is modulated by t_{Cu}, revealing an oscillatory-like behavior. This points to a Ruderman-Kittel-Kasuya-Yosida (RKKY)-type of coupling[30–32,37,38], where its amplitude is expected to oscillate as a function of the spacer's thickness, even though no change in the sign of the IEC is observed. This is a very surprising and interesting result and more details about the nature of the magnetic coupling in our samples can be

found in the supplementary section S8. Indeed, when compared with the calculated IEC values reported in Fig. 1f, the experimentally observed coupling does not follow the predicted sign change. Accordingly, the nature of the IEC in the magnetic multilayer Ni\Cu(t_{Cu})\Ni\Fe is investigated in more details in a wedged sample made of Cu(001)\Ni(12)\Cu(t_{Cu})\Ni(2)\Fe(2.5) (see supplementary section S8). The epitaxial multilayer grown on a Cu(001) single crystal shows clearly an IEC whose sign oscillates as a function of t_{Cu} (see supplementary Fig. S10). Based on this observation, the absence of a sign change of the IEC in the multilayers grown on top of MgO single crystals seems to be linked to the presence of the Ir buffer required to stabilize the PMA-Ni layer, which causes a lower quality of the epitaxial growth and possibly of the interfaces in those samples when compared to the full metallic stack. Indeed, the sign change of the interlayer coupling is the result of complex dynamics of the conduction electrons close to the Fermi surface, influenced by the interfaces of the systems. Our samples are characterized by strain accumulation due to lattice mismatch and strain relaxation across the stack which cannot be modelled by DFT, and this could be the origin of the unexpected absence of an IEC sign change in the experimental observation.

In Fig. 3c, the OOP domain state of the top magnet of five different samples is reported as a function of the Cu-thickness. Here, each data set originates from a different sample with a fixed t_{Cu}. As expected based on the results shown in Fig. 3b, very different magnetic domain configurations are observed in samples with different t_{Cu}. This is consistent with an effective magnetic field acting on the free magnet, whose strength is t_{Cu}-dependent. For t_{Cu} = 8.5 ML, we observe the free layer to have a uniform magnetization pointing down (blue), indicating a strong ferromagnetic coupling with the bottom magnet. For larger t_{Cu} up to 15.3 ML, the coupling is observed to become weaker. Indeed, we observe reversed magnetic domains pointing up (red

domains) with different size distributions for different t_{Cu}. Analyzing the magnetic images in Fig. 3c, we extract the skyrmion area distributions for the case of t_{Cu} = 11, 11.7, 13.5, 15.3 ML, as reported in Fig. 3d (details concerning the extraction of the skyrmions area distributions are reported in supplementary section S10). Assuming an ideal circular shape for the magnetic domains, we also extract the corresponding distributions of the effective skyrmion diameters ($2\sqrt{Area/\pi}$). The median values of the skyrmion area and effective diameter are reported in Fig. 3e. The effective diameter is observed to increase with increasing Cu thickness, suggesting the presence of an effective field $\mathbf{B}_{eff}$ whose amplitude decreases with increasing t_{Cu}, in the range of thicknesses here considered. It is worth mentioning that the IEC-stabilized magnetic skyrmions are observed not only in the as-grown magnetic multilayers, but also after the application of an external magnetic field of 0.5 T (see supplementary section S7 for more information).

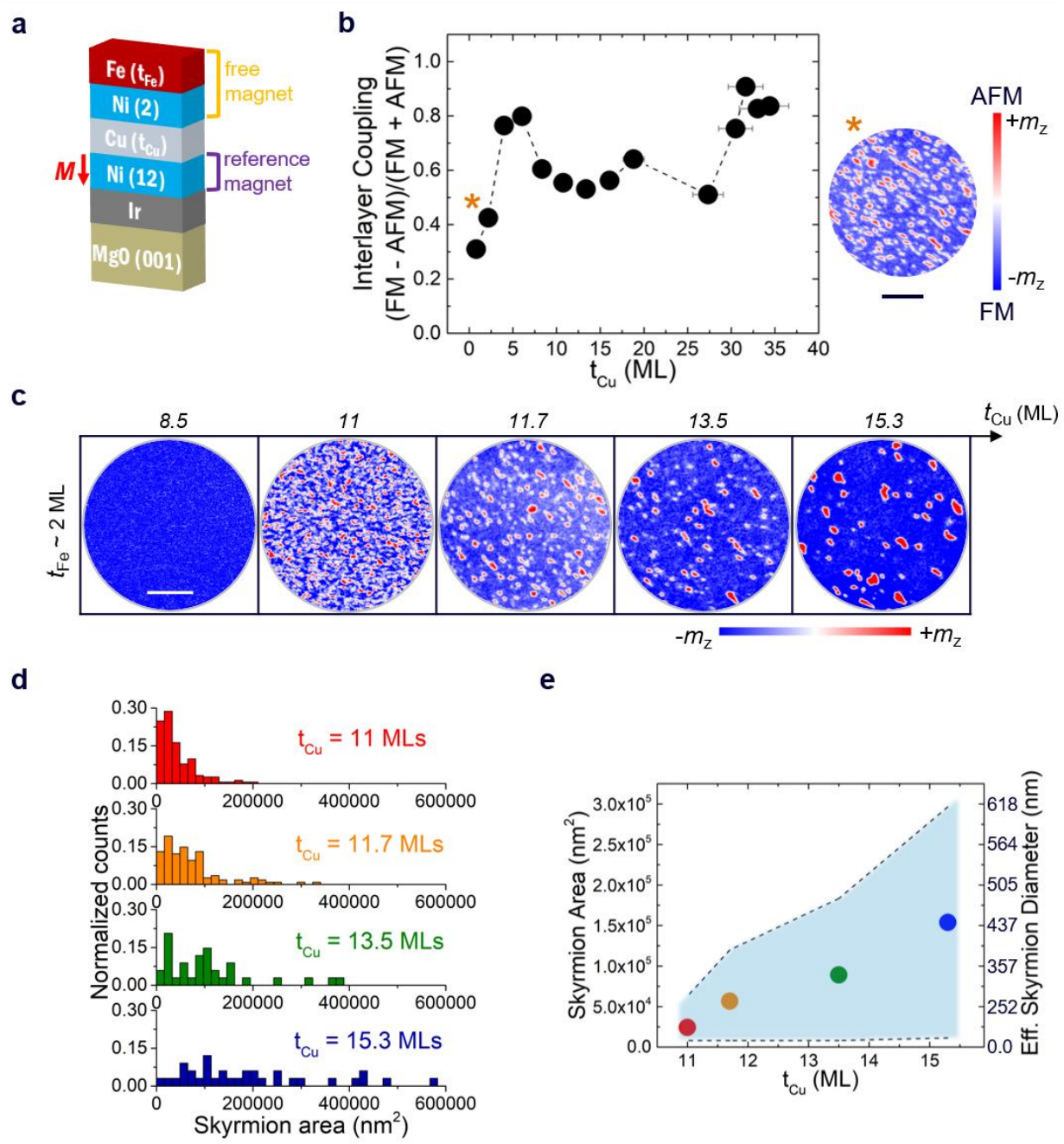

Figure 3. Tuning the properties of zero-field ferromagnetic skyrmions via IEC. a Schematic of the [001]-oriented multilayer stack investigated in this work, made of a magnetic Ni(12)-reference layer and a Ni(2)\Fe(2-2.5)-free layer. The numbers in parenthesis indicate the thickness in monolayers [ML]. The reference layer is prepared with its magnetic state pointing down (see small red arrow). **b** The essence of the interlayer coupling, determined from the normalized difference between the areas covered by domains aligned ferromagnetically (FM) and anti-ferromagnetically (AFM) with respect to the reference magnet, as a function of t_{Cu} for a sample having a wedged Cu spacer and t_{Fe} = 2.5 ML. One of the images used for such analysis is shown on the right. Scale bar is 2 µm. **c** Evolution of the OOP magnetic state in the free layer of a series of samples with different t_{Cu}. Scale bar is 2 µm. **d** Distribution of the magnetic skyrmion area for the samples with t_{Cu} = 11, 11.7, 13.5 and 15.3 ML. **e** Median values of skyrmion area and effective skyrmion diameters extracted from the histograms in panel d. The blue shaded area represents the standard deviation of the skyrmion area distributions in panel d.

A second sample with t_{Cu} = 11.7 ML and t_{Fe} = 2ML is prepared to study more in detail the spin-texture of the stabilized zero-field ferromagnetic skyrmions. Figure 4a schematically shows the complete materials stack and the experimental OOP magnetic state in the top Fe layer. Figure 4b shows an enlarged image of one of the observed skyrmions, highlighting the domain wall spin-texture. The compound SPLEEM image clearly shows a Néel-type skyrmion, with a right-handed rotational sense. In Fig. 4c we report the distribution of the orientation angle (alpha) of the DW magnetization (**m**) with respect to the normal to the DW (**n**) at all pixels located on domain wall center-lines in the image in Fig. 4a. The plot shows a single peak around alpha = 0°, indicating the presence of DWs with a Néel-character, mostly pointing from up-magnetized to down-magnetized domains, which corresponds to a right-handedness (N.R., in Fig. 4c). We point out that the handedness of the imaged DWs is in agreement with the DFT calculations above, which indeed predict the stabilization of right-handed DWs in the Cu(001)\Ni(2)\Fe(2) system, as reported in Fig. 2. Finally, Fig. 4d shows a 3D representation of the magnetization of the same skyrmion in Fig. 4b, extracted directly from the experimental data.

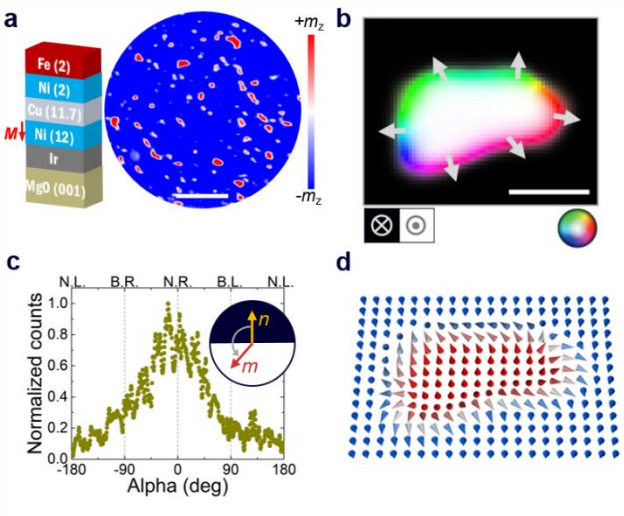

Figure 4. Skyrmion anatomy. a OOP magnetic state of a sample whose complete materials stack is shown on the left. The reference layer magnetization is pointing down, as shown by the red arrow. Scale bar is 2 µm. **b** Compound SPLEEM image of one of the observed skyrmions, showing its Néel-type right-handed chirality. The in-plane magnetization orientation is described by the color wheel. The grey arrows indicate the local magnetization direction in the DW. Scale bar is 200 nm. **c** Histogram of the DW magnetization angle distribution for the skyrmions in panel a. The single peak at alpha = 0° shows that the observed magnetic skyrmions are Néel-type with right-handed (N.R.) chirality. **d** A 3-dimentional representation of the magnetization of the skyrmion in panel b. Each cone represents a 3x3 pixel^2 area.

The study presented above shows how we can use IEC to stabilize and control the properties of ferromagnetic skyrmions at room temperature without any external magnetic field. However, applications such as magnetic data storage devices also require small (below 100 nm) dimensions of the skyrmions. With this requirement in mind, we explore a new materials system grown on top of an MgO(111) substrate. The interest in (111)-systems is justified by the fact that they offer more flexibility for the type of materials we can use. First, several (111)-textured magnetic systems have been shown to possess an OOP anisotropy[39,40], which is one of the requirements for a thin film-based skyrmionic system. Second, the majority of the reported thin-film multilayers with large DMI hosting skyrmions had a (111)-texture, with the ferromagnetic layer in direct contact with a heavy metal layer[4,17,19]. Accordingly, we use $[Co\backslash Ni]_n$ multilayers for building the two magnets and Ir for the non-magnetic spacer. [111]-oriented $[Co\backslash Ni]_n$ multilayers are known for being very useful, due to their tunable magnetic anisotropy via tailoring of the thickness ratio between the two

materials[41]. We grow a reference magnet consisting of [Ni(3)\Co(1)]$_5$\Ni(3) on top of an Ir(111) buffer layer, resulting in an OOP magnetized system. Analogously to what has been done for the (001)-system, after growth the reference magnet is saturated by a $\mu_0 \boldsymbol{H}$ = -0.5 T magnetic field, which aligns all the magnetic moments downward. After the deposition of the Ir spacer, we complete the stack by growing the free magnet consisting of a Co(5)\Ni(3)-bilayer (see the schematic in Fig. 5a).

Three different samples are investigated, with t_{Ir} = 6, 10 and 15 ML, respectively. The magnetic state of the free layer of the three samples is shown in Fig. 5b. The sample with the thinnest spacer shows a single domain state with magnetization pointing down (red color). This indicates strong ferromagnetic coupling between the reference magnet and the free magnet. The sample with intermediate spacer thickness shows the appearance of small reversed domains (blue-white) pointing up. Finally, for the thickest spacer, larger reversed domains are observed. These observations indicate the presence of an effective field $\mathbf{B}_{eff}$ which decreases with increasing t_{Ir} for the thicknesses investigated here. The skyrmion area and effective diameter distributions for t_{Ir} = 10 ML are shown in Fig. 5c and 5d, respectively. Those distributions show that a substantial portion of the skyrmions have a sub-100 nm diameter. A line profile measured from one skyrmion allows us to extract a full width at half maximum of 78 ± 3 nm via a Gaussian fit (see Fig. 5e). Figure 5f plots the relative amplitude of the OOP component of the magnetization versus position of the same skyrmion.

In order to extract the handedness of the DWs in the free magnet, we investigate the materials stack MgO(111)\Ir(10)\Co(5)\Ni(3), as shown in Fig 5g. This system shows wider DWs, which makes it easier for us to resolve their internal spin-texture. The observed DW spin-texture and the distribution of the DW magnetization orientation angle (alpha) are shown in Fig. 5g and 5h,

respectively. As visible in the histogram in Fig. 5h, the DW magnetization angle distribution has a narrow single peak around alpha = 0°, indicating that these are Néel DWs with a right-handed rotational sense.

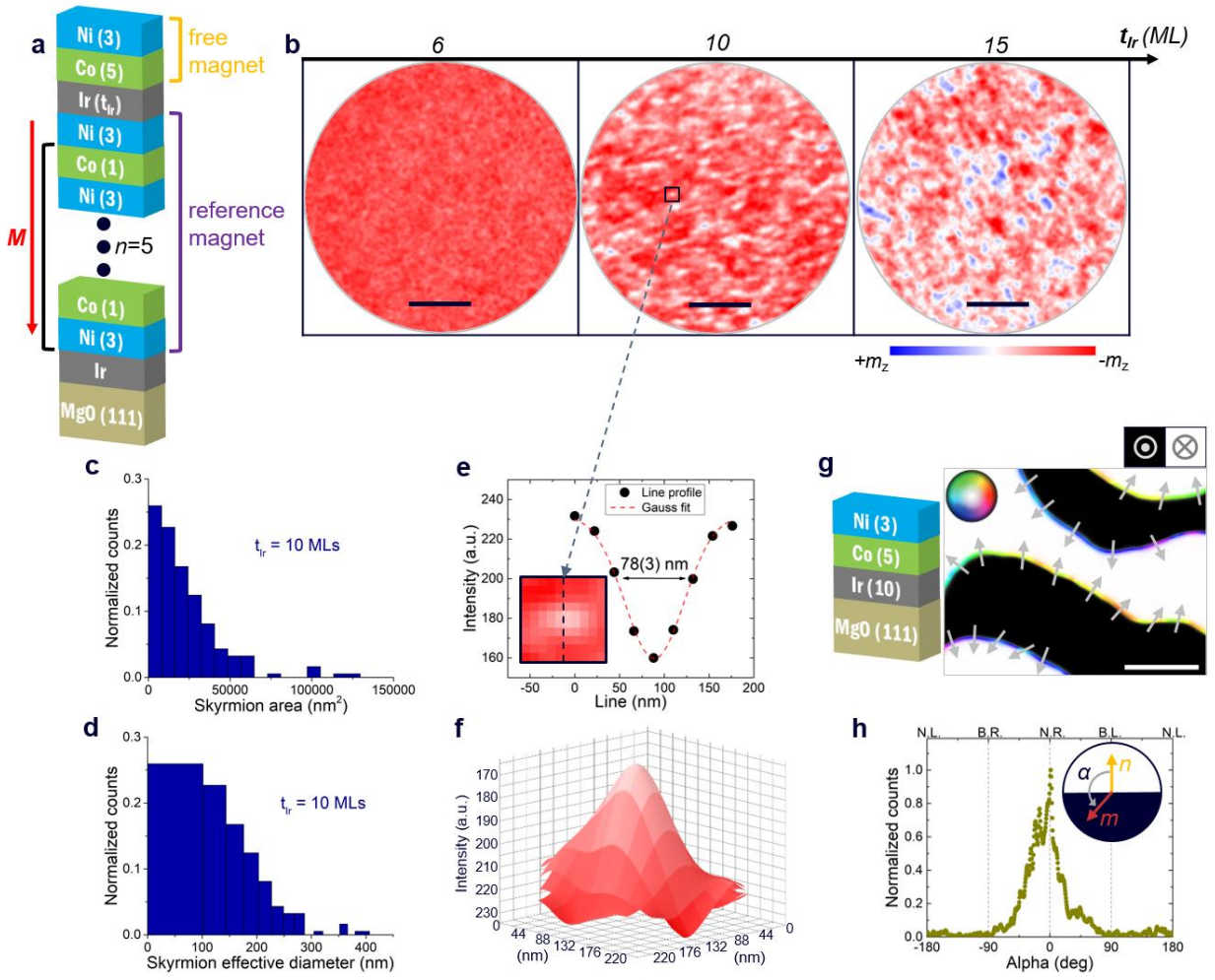

Figure 5. Sub-100 nm zero-field room temperature ferromagnetic skyrmions. a Schematic of the (111)-multilayer stacks investigated in this work, made of a magnetic [Ni(3)\Co(1)]$_5$\Ni(3) reference layer and a Co(5)\Ni(3) free layer. The numbers in parenthesis indicate individual layer thicknesses in ML. The reference layer is prepared with its magnetic state pointing down (see small red arrow). **b** Evolution of the OOP magnetic state in the free layer of three samples with different Ir-spacer thickness. Scale bar is 1 µm. **c** Distribution of the magnetic skyrmion area for the sample with t_{Ir} = 10 ML. **d** Distribution of the effective skyrmion diameter for the same sample in panel c. **e** Line profile of the relative amplitude of the OOP magnetization component across one of the observed skyrmions for t_{Ir} = 10 ML. The inset shows an enlarged image of the skyrmion. The extracted skyrmion diameter (FWHM) is 78 ± 3 nm. **f** 2D map of the relative amplitude of the OOP magnetization component of the skyrmion in panel e. **g** Schematic of the multilayer stack used to extract the DW spin-texture of the Ir\Co(5)\Ni(3) free layer. In the compound SPLEEM image the in-plane orientation of the magnetization is represented in color, as described by the color wheel, while black (white) indicates up (down) orientation of the OOP component. In addition, the grey arrows emphasize the local magnetization direction in the DWs. Scale bar is 1 µm. **h** Histogram of the DW magnetization angle distribution for the sample in panel g. The single peak at alpha = 0° indicates the presence of right-handed Néel (N.R.) domain walls.

Comparing Fig. 4c and Fig. 5h, we see that the DW magnetization angle distribution shows a much smaller width of the peak for the Ir\[Co\Ni] system (Gaussian fit width = 35°) than for the Cu\[Ni\Fe] system (width = 98°; see supplementary section S5). This is evidence of a larger DMI in Ir\[Co\Ni] than in Cu\[Ni\Fe]. Indeed, a stronger DMI results in a larger energy split between Néel and Bloch DW configurations as well as between Néel-right and Néel-left DW configurations. Accordingly, stronger DMI is expected to stabilize non-collinear spin-textures which are more robust against thermal fluctuations and pinning effects due to imperfections of the system, resulting in a narrower DW angle distribution, as reported in this work. These findings are in agreement with reports from the literature, where the experimentally extracted DMI for Ir(111)\[Co\Ni][42] was found to be three times stronger than for Cu(001)\Ni\Fe[36]. The DFT-extracted DMI for Cu(001)\Ni(2)\Fe(2) (D_{eff} = 0.16 meV per atom, see Fig. 2b) is in good agreement with the experimental value reported by G. Chen et al.[36] (0.12 – 0.17 meV per atom), validating the experimentally determined DMI of the two references above and supporting our interpretation. Furthermore, the Ir\[Co(5)\Ni(3)] system shows the possibility to nucleate smaller skyrmions than the Cu\[Ni(2)\Fe(2)] system, despite the larger dipolar energy of the former due to its larger magnetic thickness[43]. Accordingly, the Ir-based stack will be more suitable for applications requiring small and stable isolated skyrmions in the absence of external magnetic fields at room temperature.

In summary, our results show that interlayer exchange coupling (IEC) between a reference and a free magnet can be a powerful tool for stabilizing and tailoring room-temperature isolated ferromagnetic skyrmions without any magnetic field. These multilayers are grown by epitaxy on insulating MgO substrates, which is an important step towards the development of spintronic devices based on zero-field room temperature magnetic skyrmions. Furthermore, the size and the

areal density of the nucleated skyrmions can be tuned by tailoring the thickness of the non-magnetic spacer in between the two magnetic layers. By carefully choosing the materials of the spacer and of the magnets, sub-100 nm ferromagnetic skyrmions can be stabilized at zero-field. This work highlights the possibility to use IEC for the development of skyrmion-based spintronic devices where the tuning of the skyrmion size and areal density across the chip area is desired.

ASSOCIATED CONTENT

Supporting Information.

The following files are available free of charge…

More details about: samples preparation; DFT calculations; 3D vector magnetic imaging via spin-polarized low energy electron microscopy (PDF)

AUTHOR INFORMATION

Corresponding Author

*E-mail: rloconte.magnetism@gmail.com (R.L.C.)

*E-mail: aknandy@niser.ac.in (A.K.N.)

*E-mail: AKSchmid@lbl.gov (A.K.S.)

*E-mail: wiesendanger@physnet.uni-hamburg.de (R.W.)

ORCID

Roberto Lo Conte: 0000-0002-5050-9978

Author Contributions

R.L.C. and A.K.N. prepared the manuscript. R.L.C., A.K.N., A.K.S. and R.W. conceived the study. A.K.N. and A.M. performed, analyzed and interpreted the ab-initio DFT calculations. R.L.C., with the support of A.L.F.C, carried out the SPLEEM measurements. R.L.C., C.O., A.L.F.C. and G.C. analyzed and interpreted the SPLEEM results. Z.J.C., K.L. and A.T.N. carried out magnetic characterizations and helped interpreting SPLEEM results. All authors discussed the results and commented on the manuscript.

ACKNOWLEDGMENT

R.L.C., A.K.S. and R.W. acknowledge financial support by the European Union via an International Marie Skłodowska-Curie Fellowship (grant No. 748006 - SKDWONTRACK). A.L.F.C. and A.K.S. acknowledge the support by the Advanced Research Projects Agency-Energy (ARPA-E), U.S. Department of Energy, under Award Number DE-AR0000664. C.O. acknowledges support from the US Department of Energy Early Career Research Program. G.C., Z.J.C. and K.L. acknowledge support from the US NSF (DMR-1610060 and DMR-1905468) and the UCOP Multicampus Research Programs and Initiatives (MRP-17-454963). The Magnetic Property Measurements System (MPMS3) at Georgetown University used herein was supported by the NSF (DMR-1828420). A.K.N. and A.M. acknowledge financial support from the Department of Atomic Energy, Government of India. A.K.N. thanks Prof. P. M. Oppeneer for the Swedish National Infrastructure for Computing (SNIC) facility. A.K.N. also thanks Dr. Gustav Bihlmayer for the computational support, JURECA at JSC, Forschungszentrum, JÜLICH. Work at the Molecular Foundry and at the Advanced Light Source was supported by the Office of Science, Office of Basic Energy Sciences, of the US Department of Energy under contract no. DE-AC02-05CH11231.

REFERENCES

(1) Bogdanov, A.; Hubert, A. Thermodynamically Stable Magnetic Vortex States in Magnetic

Crystals. *J. Magn. Magn. Mater.* **1994**, *138* (3), 255–269. https://doi.org/10.1016/0304-8853(94)90046-9.

(2) Rößler, U. K.; Bogdanov, A. N.; Pfleiderer, C. Spontaneous Skyrmion Ground States in Magnetic Metals. *Nature* **2006**, *442* (7104), 797–801. https://doi.org/10.1038/nature05056.

(3) Mühlbauer, S.; Binz, B.; Jonietz, F.; Pfleiderer, C.; Rosch, A.; Neubauer, A.; Georgii, R.; Böni, P. Skyrmion Lattice in a Chiral Magnet. *Science (80-.).* **2009**, *323* (5916), 915–919. https://doi.org/10.1126/SCIENCE.1166767.

(4) Romming, N.; Hanneken, C.; Menzel, M.; Bickel, J. E.; Wolter, B.; von Bergmann, K.; Kubetzka, A.; Wiesendanger, R. Writing and Deleting Single Magnetic Skyrmions. *Science (80-.).* **2013**, *341* (August), 636–639. https://doi.org/10.1038/nphys2045.

(5) Fert, A.; Levy, P. M. Role of Anisotropic Exchange Interactions in Determining the Properties of Spin-Glasses. *Phys. Rev. Lett.* **1980**, *44* (23), 1538–1541. https://doi.org/10.1103/PhysRevLett.44.1538.

(6) Fert, A. Magnetic and Transport Properties of Metallic Multilayers. *Mater. Sci. Forum* **1991**, *59–60*, 440–480. https://doi.org/10.4028/www.scientific.net/MSF.59-60.439.

(7) Crépieux, A.; Lacroix, C. Dzyaloshinsky–Moriya Interactions Induced by Symmetry Breaking at a Surface. *J. Magn. Magn. Mater.* **1998**, *182* (3), 341–349. https://doi.org/10.1016/S0304-8853(97)01044-5.

(8) Vedmedenko, E. Y.; Udvardi, L.; Weinberger, P.; Wiesendanger, R. Chiral Magnetic Ordering in Two-Dimensional Ferromagnets with Competing Dzyaloshinsky-Moriya Interactions. *Phys. Rev. B* **2007**, *75* (10), 104431. https://doi.org/10.1103/PhysRevB.75.104431.

(9) Bode, M.; Heide, M.; Von Bergmann, K.; Ferriani, P.; Heinze, S.; Bihlmayer, G.; Kubetzka, A.; Pietzsch, O.; Blügel, S.; Wiesendanger, R. Chiral Magnetic Order at Surfaces Driven by Inversion Asymmetry. *Nature* **2007**, *447* (7141), 190–193. https://doi.org/10.1038/nature05802.

(10) Chen, G.; Schmid, A. K. Imaging and Tailoring the Chirality of Domain Walls in Magnetic Films. *Adv. Mater.* **2015**, *27* (38), 5738–5743. https://doi.org/10.1002/adma.201500160.

(11) Zhang, X.; Cai, W.; Zhang, X.; Wang, Z.; Li, Z.; Zhang, Y.; Cao, K.; Lei, N.; Kang, W.; Zhang, Y.; et al. Skyrmions in Magnetic Tunnel Junctions. *ACS Appl. Mater. Interfaces* **2018**, *10* (19), 16887–16892. https://doi.org/10.1021/acsami.8b03812.

(12) Li, S.; Kang, W.; Huang, Y. Magnetic Skyrmion-Based Synaptic Devices Magnetic Skyrmion-Based Artificial Neuron Device. *Nanotechnology* **2017**, *28*, 08LT02.

(13) Prychynenko, D.; Sitte, M.; Litzius, K.; Krüger, B.; Bourianoff, G.; Kläui, M.; Sinova, J.; Everschor-Sitte, K. Magnetic Skyrmion as a Nonlinear Resistive Element: A Potential Building Block for Reservoir Computing. *Phys. Rev. Appl.* **2018**, *9* (1), 014034. https://doi.org/10.1103/PhysRevApplied.9.014034.

(14) Yu, G.; Upadhyaya, P.; Shao, Q.; Wu, H.; Yin, G.; Li, X.; He, C.; Jiang, W.; Han, X.; Amiri, K.; et al. Room-Temperature Skyrmion Shift Device for Memory Application. *Nano Lett.* **2017**, *17*, 261–268. https://doi.org/10.1021/acs.nanolett.6b04010.

(15) Büttner, F.; Moutafis, C.; Schneider, M.; Krüger, B.; Günther, C. M.; Geilhufe, J.; Schmising, C. v. K.; Mohanty, J.; Pfau, B.; Schaffert, S.; et al. Dynamics and Inertia of Skyrmionic Spin Structures. *Nat. Phys.* **2015**, *11* (3), 225–228. https://doi.org/10.1038/nphys3234.

(16) Jiang, W.; Upadhyaya, P.; Zhang, W.; Yu, G.; Jungfleisch, M. B.; Fradin, F. Y.; Pearson, J. E.; Tserkovnyak, Y.; Wang, K. L.; Heinonen, O.; et al. Blowing Magnetic Skyrmion Bubbles. *Science* **2015**, *349* (6245), 283. https://doi.org/10.1126/science.aaa1442.

(17) Moreau-Luchaire, C.; Moutafis, C.; Reyren, N.; Sampaio, J.; Vaz, C. A. F.; Van Horne, N.; Bouzehouane, K.; Garcia, K.; Deranlot, C.; Warnicke, P.; et al. Additive Interfacial Chiral Interaction in Multilayers for Stabilization of Small Individual Skyrmions at Room Temperature. *Nat. Nanotechnol.* **2016**, *11* (5), 444–448. https://doi.org/10.1038/nnano.2015.313.

(18) Woo, S.; Litzius, K.; Krüger, B.; Im, M.-Y.; Caretta, L.; Richter, K.; Mann, M.; Krone, A.; Reeve, R. M.; Weigand, M.; et al. Observation of Room-Temperature Magnetic Skyrmions and Their Current-Driven Dynamics in Ultrathin Metallic Ferromagnets. *Nat. Mater.* **2016**, *15* (5), 501–506. https://doi.org/10.1038/nmat4593.

(19) Soumyanarayanan, A.; Raju, M.; Gonzalez Oyarce, A. L.; Tan, A. K. C.; Im, M.-Y.; Petrović, A. P.; Ho, P.; Khoo, K. H.; Tran, M.; Gan, C. K.; et al. Tunable Room-Temperature Magnetic Skyrmions in Ir/Fe/Co/Pt Multilayers. *Nat. Mater.* **2017**, *16* (9), 898–904. https://doi.org/10.1038/nmat4934.

(20) Woo, S.; Song, K. M.; Zhang, X.; Ezawa, M.; Zhou, Y.; Liu, X.; Weigand, M.; Finizio, S.; Raabe, J.; Park, M.-C.; et al. Deterministic Creation and Deletion of a Single Magnetic Skyrmion Observed by Direct Time-Resolved X-Ray Microscopy. *Nat. Electron.* **2018**, *1* (5), 288–296. https://doi.org/10.1038/s41928-018-0070-8.

(21) Caretta, L.; Mann, M.; Büttner, F.; Ueda, K.; Pfau, B.; Günther, C. M.; Hessing, P.; Churikova, A.; Klose, C.; Schneider, M.; et al. Fast Current-Driven Domain Walls and Small Skyrmions in a Compensated Ferrimagnet. *Nat. Nanotechnol.* **2018**, *13* (12), 1154–

1160. https://doi.org/10.1038/s41565-018-0255-3.

(22) Zhang, X.; Ezawa, M.; Zhou, Y. Magnetic Skyrmion Logic Gates: Conversion, Duplication and Merging of Skyrmions. *Sci. Rep.* **2015**, *5*. https://doi.org/10.1038/srep09400.

(23) Gilbert, D. A.; Maranville, B. B.; Balk, A. L.; Kirby, B. J.; Fischer, P.; Pierce, D. T.; Unguris, J.; Borchers, J. A.; Liu, K. Realization of Ground-State Artificial Skyrmion Lattices at Room Temperature. *Nat. Commun.* **2015**, *6* (1), 8462. https://doi.org/10.1038/ncomms9462.

(24) Boulle, O.; Vogel, J.; Yang, H.; Pizzini, S.; De Souza Chaves, D.; Locatelli, A.; Menteş, T. O.; Sala, A.; Buda-Prejbeanu, L. D.; Klein, O.; et al. Room-Temperature Chiral Magnetic Skyrmions in Ultrathin Magnetic Nanostructures. *Nat. Nanotechnol.* **2016**, *11* (5), 449–454. https://doi.org/10.1038/nnano.2015.315.

(25) Chen, G.; Mascaraque, A.; N'Diaye, A. T.; Schmid, A. K. Room Temperature Skyrmion Ground State Stabilized through Interlayer Exchange Coupling. *Appl. Phys. Lett.* **2015**, *106* (24), 242404. https://doi.org/10.1063/1.4922726.

(26) Lemesh, I.; Litzius, K.; Böttcher, M.; Bassirian, P.; Kerber, N.; Heinze, D.; Zázvorka, J.; Büttner, F.; Caretta, L.; Mann, M.; et al. Current-Induced Skyrmion Generation through Morphological Thermal Transitions in Chiral Ferromagnetic Heterostructures. *Adv. Mater.* **2018**, 1805461. https://doi.org/10.1002/adma.201805461.

(27) Yu, G.; Jenkins, A.; Ma, X.; Razavi, S. A.; He, C.; Yin, G.; Shao, Q.; He, Q. lin; Wu, H.; Li, W.; et al. Room-Temperature Skyrmions in an Antiferromagnet-Based Heterostructure. *Nano Lett.* **2018**, *18* (2), 980–986. https://doi.org/10.1021/acs.nanolett.7b04400.

(28) Brandão, J.; Dugato, D. A.; Seeger, R. L.; Denardin, J. C.; Mori, T. J. A.; Cezar, J. C. Observation of Magnetic Skyrmions in Unpatterned Symmetric Multilayers at Room Temperature and Zero Magnetic Field. *Sci. Rep.* **2019**, *9* (1), 4144. https://doi.org/10.1038/s41598-019-40705-4.

(29) Nandy, A. K.; Kiselev, N. S.; Blügel, S. Interlayer Exchange Coupling: A General Scheme Turning Chiral Magnets into Magnetic Multilayers Carrying Atomic-Scale Skyrmions. *Phys. Rev. Lett.* **2016**, *116*, 177202. https://doi.org/10.1103/PhysRevLett.116.177202.

(30) Gruenberg, P.; Schreiber, R.; Pang, Y.; Brodsky, M. B.; Sowers, H. Layered Magnetic Structures: Evidence for Antiferromagnetic Coupling of Fe Layers across Cr Interlayers. *Phys. Rev. Lett.* **1986**, *57* (19), 2442–2445. https://doi.org/10.1103/PhysRevLett.57.2442.

(31) Parkin, S. S. P.; Bhadra, R.; Roche, K. P. Oscillatory Magnetic Exchange Coupling through Thin Copper Layers. *Phys. Rev. Lett.* **1991**, *66* (16), 2152–2155. https://doi.org/10.1103/PhysRevLett.66.2152.

(32) Bruno, P.; Chappert, C. INTERLAYER EXCHANGE COUPLING: RKKY THEORY AND BEYOND. In *Magnetism and Structure in Systems of Reduced Dimentions*; R.F.C. Farrow et al., Ed.; Plenum Press: New York, 1993; pp 389–399.

(33) Kresse, G.; Hafner, J. *Ab Initio* Molecular Dynamics for Liquid Metals. *Phys. Rev. B* **1993**, *47* (1), 558–561. https://doi.org/10.1103/PhysRevB.47.558.

(34) Kresse, G.; Furthmüller, J. Efficient Iterative Schemes for Ab Initio Total-Energy Calculations Using a Plane-Wave Basis Set. *Phys. Rev. B - Condens. Matter Mater. Phys.* **1996**, *54* (16), 11169–11186. https://doi.org/10.1103/PhysRevB.54.11169.

(35) Wimmer, E.; Krakauer, H.; Weinert, M.; Freeman, A. J. Full-Potential Self-Consistent

Linearized-Augmented-Plane-Wave Method for Calculating the Electronic Structure of Molecules and Surfaces: O2 Molecule. *Phys. Rev. B* **1981**, *24* (2), 864–875. https://doi.org/10.1103/PhysRevB.24.864.

(36) Chen, G.; Zhu, J.; Quesada, A.; Li, J.; N'Diaye, A. T.; Huo, Y.; Ma, T. P.; Chen, Y.; Kwon, H. Y.; Won, C.; et al. Novel Chiral Magnetic Domain Wall Structure in Fe / Ni / Cu (001) Films. *Phys. Rev. Lett.* **2013**, *110* (17), 177204. https://doi.org/10.1103/PhysRevLett.110.177204.

(37) Qiu, Z. Q.; Pearson, J.; Bader, S. D. Oscillatory Interlayer Magnetic Coupling of Wedged Co/Cu/Co Sandwiches Grown on Cu(100) by Molecular Beam Epitaxy. *Phys. Rev. B* **1992**, *46* (13), 8659–8662. https://doi.org/10.1103/PhysRevB.46.8659.

(38) Bruno, P.; Chappert, C. Oscillatory Coupling between Ferromagnetic Layers Separated by a Nonmagnetic Metal Spacer. *Phys. Rev. Lett.* **1991**, *67* (12), 1602–1605. https://doi.org/10.1103/PhysRevLett.67.1602.

(39) Arora, M.; Hübner, R.; Suess, D.; Heinrich, B.; Girt, E. Origin of Perpendicular Magnetic Anisotropy in Co/Ni Multilayers. *Phys. Rev. B* **2017**, *96* (2), 024401. https://doi.org/10.1103/PhysRevB.96.024401.

(40) Gambardella, P.; Rusponi, S.; Veronese, M.; Dhesi, S. S.; Grazioli, C.; Dallmeyer, A.; Cabria, I.; Zeller, R.; Dederichs, P. H.; Kern, K.; et al. Giant Magnetic Anisotropy of Single Cobalt Atoms and Nanoparticles. *Science* **2003**, *300* (5622), 1130–1133. https://doi.org/10.1126/science.1082857.

(41) Andrieu, S.; Hauet, T.; Gottwald, M.; Rajanikanth, A.; Calmels, L.; Bataille, A. M.; Montaigne, F.; Mangin, S.; Otero, E.; Ohresser, P.; et al. Co/Ni Multilayers for Spintronics: High Spin Polarization and Tunable Magnetic Anisotropy. *Phys. Rev. Mater.*

2018, *2* (6), 064410. https://doi.org/10.1103/PhysRevMaterials.2.064410.

(42) Chen, G.; N'Diaye, A. T.; Wu, Y.; Schmid, A. K. Ternary Superlattice Boosting Interface-Stabilized Magnetic Chirality. *Appl. Phys. Lett.* **2015**, *106* (6), 062402. https://doi.org/10.1063/1.4907889.

(43) Büttner, F.; Lemesh, I.; Beach, G. S. D. Theory of Isolated Magnetic Skyrmions: From Fundamentals to Room Temperature Applications. *Sci. Rep.* **2018**, *8* (1), 4464. https://doi.org/10.1038/s41598-018-22242-8.